IAC-22-68573

An Advanced Tool to Determine the Apparent Rotation Period of a Space Object from a Fusion of Measurements

G. Quint[a], A. de Andrés[a]*, M. Viturro[a], J. Carro[a], V. Morand[b], M. Steindorfer et al.[c]

[a] *GMV Innovating Solutions SARL, 17 rue Hermès, Ramonville-Saint-Agne, France 31520,* guillaume.quint@gmv.com, adandres@gmv.com, mviturro@gmv.com, jcarro@gmv.com
[b] *Centre National d'Etudes Spatiales, 18 avenue Edouard Belin, Toulouse, France 31400,* vincent.morand@cnes.fr
[c] *Space Research Institute, Austrian Academy of Sciences, 6 Schmiedlstraße, Graz, Austria 8042,* michael.steindorfer@oeaw.ac.at, georg.kirchner@oeaw.ac.at, peiyuan.wang@oeaw.ac.at
* Corresponding Author

Abstract

Determining the attitude of a space object from space situational awareness (SSA) data is interesting for several applications such as contingency operations in case of loss of signal from a satellite, support to active debris removal missions or characterization of unknown objects. A first step in this determination process is to detect whether the satellite is rotating or not and estimate its rotation period.

This paper presents the results of a CNES R&D activity performed by GMV to develop a robust and automated way of determining the apparent rotation period of a satellite by fusing different types of SSA measurements: telescope and laser light curves, radar cross section and laser range measurements (for cooperative objects equipped with a retroreflector). The process is based on the computation of a Lomb-Scargle periodogram, allowing to detect all possible candidates for the rotation frequency, and an iterative epoch folding method on each candidate to optimize its frequency. The selection of the real rotation frequency within the list of optimized candidates is based on the comparison of their folding error.

Lomb-Scargle periodogram has already been used to estimate the rotation period of space objects in previous publications (Balachandran, K. et Subbarao, K. *Estimating Sidereal rotation period of Resident Space Objects using non-uniformly sampled light curves.* 2018), but only applied to a single type of measurement and retaining the most powerful frequency as the real rotation one. The advantage of fusing measurements is presented in this paper. It will be shown that it helps removing spurious frequencies from the periodogram, emphasizing the real rotation frequency of the object and its eventual harmonics.

Using epoch folding method to optimize candidates and folding error to select the best candidate for the real rotation frequency has been proposed in the past (Cognion, Rita L. *Rotation rates of inactive satellites near geosynchronous earth orbit.* 2014), but always using the whole set of measurements. An upgrade to this approach consists in using the best interval of measurements (the one with the best compromise of low noise and high data density) with a limited duration (two or three candidate periods). The advantage of using this approach is a drastic reduction of the ambiguity when comparing the folding error of optimized candidates, allowing a more confident selection of the best candidate for the real rotation frequency.

The tool where these methods have been implemented (*GLADIATOR*) has been tested with simulated measurements, but also with real measurements obtained during an observations campaign and comparing results with external sources. The obtained results show the validity of the proposed methodology and the associated tool to successfully determine the rotation period of space objects through SSA data fusion.
Keywords: Space debris, rotation state, data fusion, periodogram, epoch folding.

1. Introduction

The GLADIATOR tool (*Generator of Light, Area and DIstance measurements and ATtitude determinatOR*) implemented in this work allows to determine the rotation state of an object. Information about whether the object is in rotation or 3-axis stabilized, as well as the synodic rotation period of rotating objects, are retrieved from different type of measurements (classic and laser light curves, radar cross-section and laser range residuals) all together (data fusion). It is important to note that laser range residuals (issued from a previous orbit determination process) can only be exploited for these purposes if the object is equipped with a retroreflector, because in other case the variations in the residuals will not reflect attitude changes, as the laser beam could be reflected by a different part of the object at every instant.

The tool uses the whole set of input measurements, instead of a single type of data (classic light curve in [1,2,4] and laser ranging in [5,6]), to produce a Lomb-Scargle periodogram. Even if the patterns found in each

type of data are completely different, their repetition frequency should be the same if they correspond to the real synodic rotation frequency of the object or one of its harmonics. So, this data fusion in the Lomb-Scargle periodogram can only make the peaks corresponding to the real synodic rotation frequency and their harmonics more powerful and the spurious peaks less powerful.

The peaks in the periodogram are then automatically detected by the tool and they are all considered as candidates for the real synodic rotation period of the object. However, due to measurements noise and sampling, these peaks can be biased, so an optimization of candidates is required to refine their value. This optimization is performed by an iterative epoch folding method [3,4], using an optimization criterion based on the standard deviation of folded data with respect to a mean folded signal (folding error). As epoch folding can only be performed on a single type of data, because it is based in the reconstruction of a pattern in a signal, data fusion is applied here in the sense that it is the tool who is automatically selecting, from the whole set of input data, the most suited interval of a single type of data for the optimization process (folding interval). The selection criterion is based on the density, variability and noise of the data.

Finally, the candidate corresponding to the real synodic rotation period of the object is not always the most powerful in the periodogram (as considered in [1,4,5,6]) or the one corresponding to the lowest harmonic (as considered in [2]), so another way of determining the best candidate is required. This work proposes using the normalized folding error for this purpose (normalizing with data noise), as the best candidate should have the lowest value of this parameter. Normalized value allows to compare candidates that have been optimized using different types of data. However, one could always find peaks in the periodogram even if the object is 3-axis stabilized, so another criterion is added to determine whether the object is in rotation: the best candidate must have at least one harmonic within the list of optimized candidates or must be a harmonic of another optimized candidate.

2. Selecting candidates with data fusion

As argued in the introduction, Lomb-Scargle periodogram is computed using the whole set of input data (classic light curves, RCS, laser light curve and/or laser range residuals) to add the contribution of the different types of data. This allows to emphasize the real rotation frequency of the object and some of its harmonics (see Fig. 1) or to keep the best contribution from the different types of data.

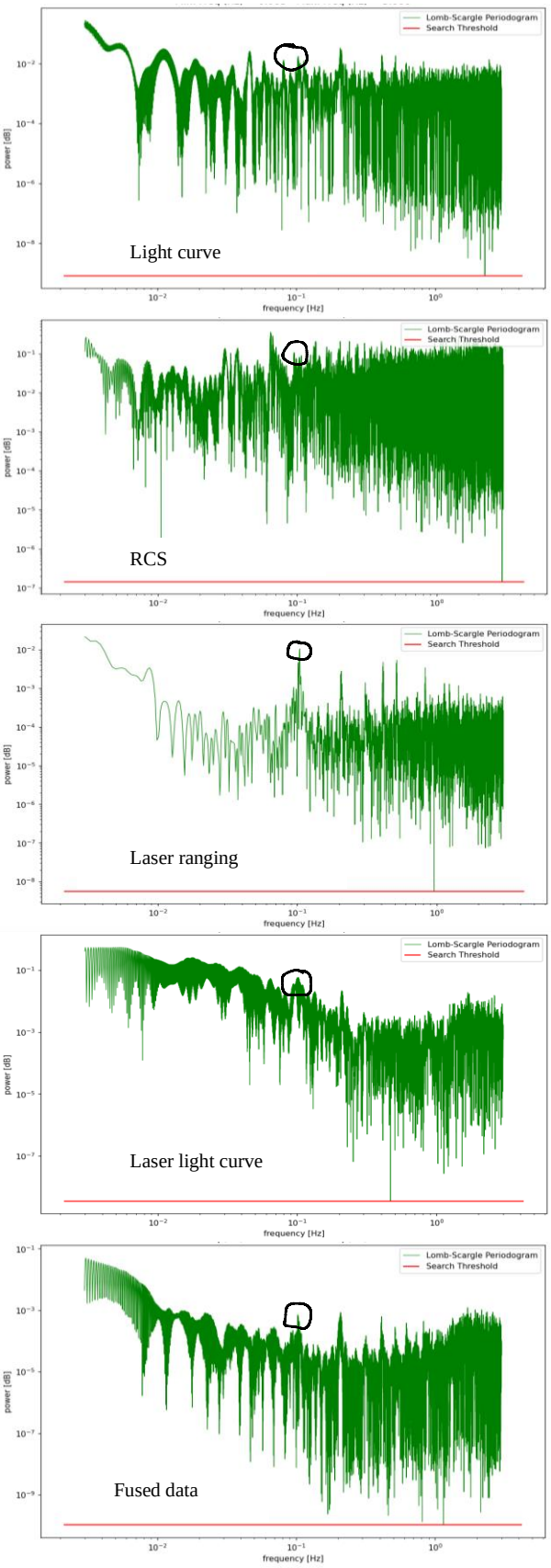

Fig. 1. Lomb-Scargle periodogram of Topex obtained with different types of data and with a fusion of these data from the observation campaign on 22nd Mars 2022. Classic light curve and RCS measurements do not reveal a clear peak at the expected rotation period (~10s from [12]), while laser light curve reveal a weak peak and a harmonic (x2). Laser range measurements produce a very good periodogram, with a heavy peak at the expected frequency and two harmonics (x2, x4), but also with two spurious harmonics (x3, x5). Fused data allows to produce the clearest periodogram, with a clear peak at the expected frequency and two harmonics (x2, x4).

RCS measurements and laser light curves are very sensitive to specular reflections, and this turns into powerful peaks in the signal (see Fig. 2). However, the rest of the signal is seen as a noise, and this adds spurious peaks in the periodogram at high frequencies. To remove these spurious peaks, a Butterworth's filter is applied to RCS and laser light curves signals before building the periodogram. This type of low-pass filter allows to remove high frequency noise from a signal (over a cut-off frequency, f_{co}) to build a smoothed signal, and is configured through two parameters: the order of the filter (n) and the Nyquist's ratio (N_r), with

$$N_r = \frac{f_{co}}{f_N}$$

, where f_N is the Nyquist's frequency, which is equal to half the sampling frequency of the signal. The empirical configuration retained to filter RCS is $n = 2$ and $N_r = 0.0001$, and $n = 2$ and $N_r = 0.07$ to filter laser light curve. It has been defined after a graphical analysis of the effect of different filter configurations to retain the real rotation frequency of several objects while removing noise as much as possible. The effect of this filter in the periodogram is shown in Fig. 2.

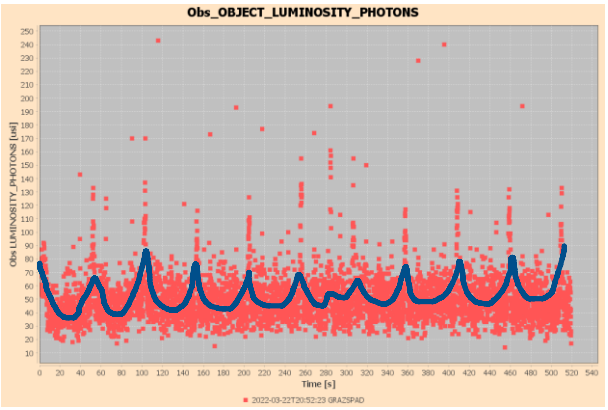

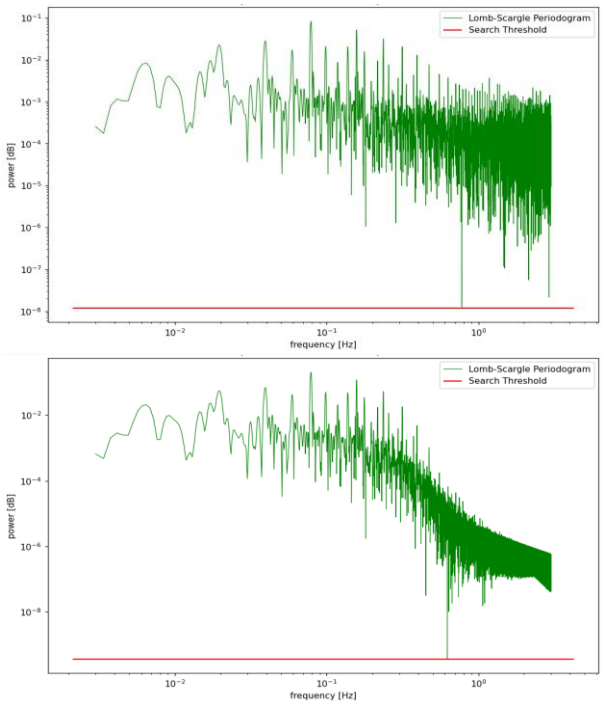

Fig. 2. Laser light curve of satellite G88 (in tumbling at ~50 s, [12]) and Butterworth's filter (blue on top plot). Comparison of first periodogram (obtained with raw data, middle plot) with second periodogram (obtained with filtered data, bottom plot) shows the disappearing of high frequency peaks from the periodogram.

All local maxima in the periodogram are detected, ordered by frequency and then filtered, as because of noise several local maxima can be part of the same peak (see Fig. 3). This filter is based on the frequency ratio and the power difference of two consecutive maxima: if frequency ratio is lower than 1.5 (so maxima cannot be harmonics of each other), then the less powerful is rejected. Finally, only the *n* most powerful peaks remaining are kept and constitute the list of candidates to be analysed.

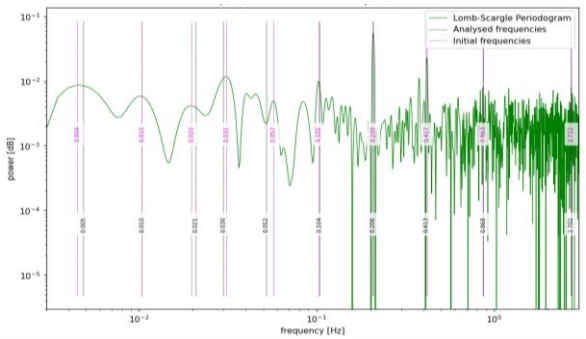

Fig. 3. Selected candidates (initial frequencies in plot) and optimized candidates (analysed frequencies in plot) in a periodogram of Topex (in tumbling at ~10s, [12]) obtained with a classic light curve.

3. Optimizing candidates with data fusion

The optimization of candidates is performed through an iterative epoch folding on an interval of data of a single data type (classic light curve, RCS, laser light curve or laser range residuals). Data must be detrended before folding using a parabolic fitting to minimize the artificial folding error due to the mean trending of data (see Fig. 4). The duration of the folding interval must also be fixed by user to 3-5 times the candidate period to optimize in order to reduce this artificial error.

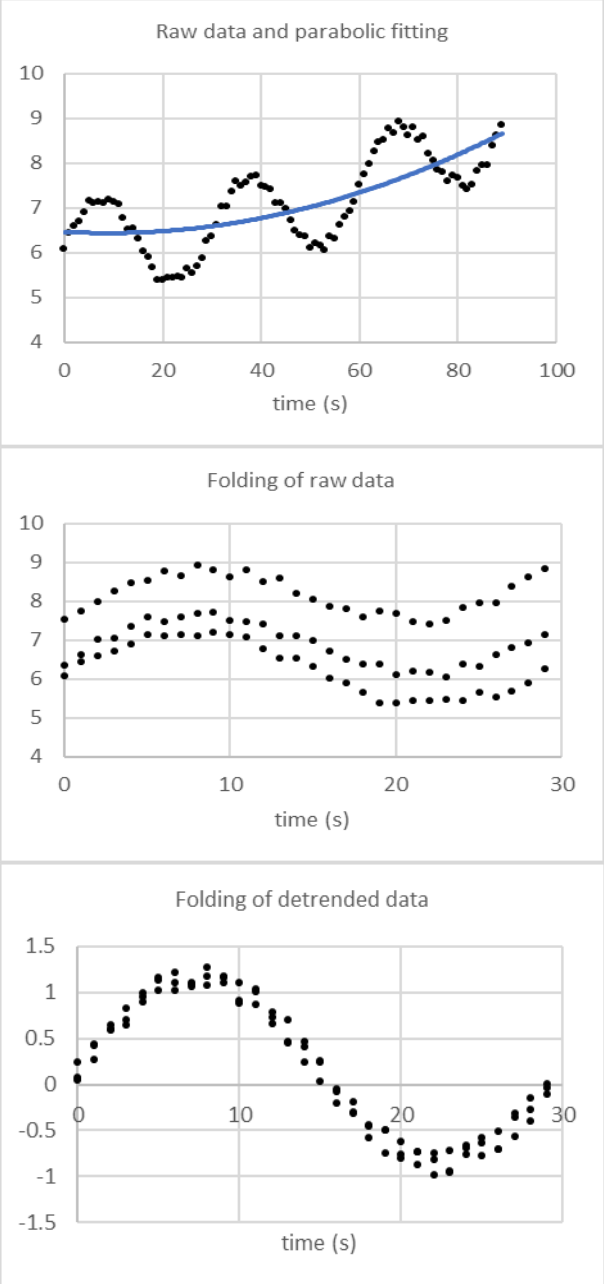

Fig. 4. Simulated light curve of a rotating object with a 30 s period and the corresponding epoch folding on raw and detrended data.

The automatic selection of the folding interval within the whole set of input data is based on the maximization of a criterion involving data density (ρ_d), standard deviation ($\sigma_d[\mu]$, where μ is the mean value of data) and noise ($\sigma_d[\mu(t)]$, defined as the standard deviation with respect to a mean signal, $\mu(t)$):

$$interval\ selection = \max\left(\frac{\rho_d \times \sigma_d[\mu_d]}{\sigma_d[\mu_d(t)]}\right)$$

Mean signal is defined here by a Butterworth's filter (see Fig. 5). The empirical configuration of this filter for the different type of data is as follows:

- Classic light curve: $n = 4$ and $N_r = 0.5$.
- RCS: $n = 2$ and $N_r = 0.1$.
- Laser light curve: $n = 2$ and $N_r = 0.1$.
- Laser range residuals: $n = 6$ and $N_r = 0.6$.

These configurations have been defined after a graphical analysis of the effect of different filter configurations to retain the mean signal of several real objects while removing noise as much as possible.

The automated iterative epoch folding uses a convergence criterion based on the minimization of the folding error, which is defined here as the noise of folded data with respect to the mean folded signal ($\varepsilon_f = \sigma_{fd}[\mu_{fd}(t)]$):

$$folding\ convergence = \min\left(\sigma_{fd}[\mu_{fd}(t)]\right)$$

Mean folded signal is again obtained with a Butterworth's filter of the folded data (see Fig. 5). The empirical configuration of this filter for the different type of data is as follows:

- Classic light curve: $n = 4$ and $N_r = 0.1$.
- RCS: $n = 2$ and $N_r = 0.03$.
- Laser light curve: $n = 2$ and $N_r = 0.05$.
- Laser range residuals: $n = 6$ and $N_r = 0.6$.

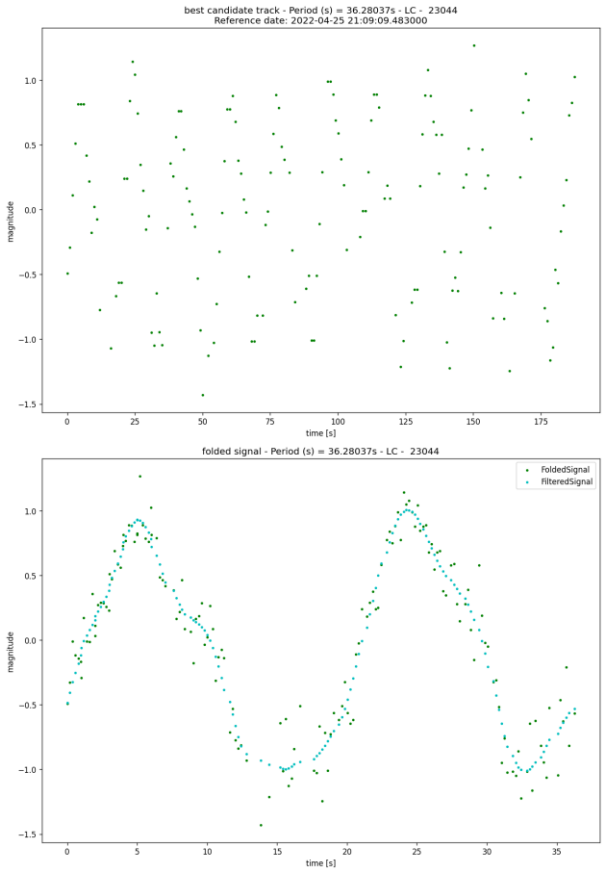

Fig. 5. Detrended light curve of COSMOS 2277 satellite in tumbling at 36.28 s and epoch folding showing mean folded data obtained with Butterworth's filter.

4. Comparing candidates with data fusion

Assuming that the most suitable candidate for the real synodic rotation period of the object is the most powerful in the periodogram or the one associated with the lowest harmonic of a series of harmonics (as in previous works) is not always valid, as can be seen in Fig. 3 for Topex: real rotation frequency is ~0.1Hz [12], but the corresponding peak is weaker than the peak of the second harmonic (~0.2 Hz) and is not the first harmonic in a sequence, as another peak is found at ~0.05 Hz.

This is why in this work the selection of the best candidate is based on the folding error, as proposed in [3,4]. However, as each candidate could be optimized here using a different type of data, a normalization of the folding error is required in order to have a comparable value. Normalized folding error (ε_f) is defined here as the folding error divided by data noise:

$$\bar{\varepsilon_f} = \frac{\varepsilon_f}{\sigma_d[\mu_d(t)]} \geq 1$$

As theoretically folding error cannot be lower than data noise, best candidate for real synodic rotation period is assumed to be the one returning the lowest value of normalized folding error (see Fig. 6).

An important limitation of the Lomb-Scargle periodogram is the impossibility to state whether the satellite is in rotation or not as peaks can be found in both cases (mainly because of random repetitive patterns found within measurements noise). To solve this problem, the notion of a sequence of harmonics relating some of the candidate when the object is in rotation [2] is used here to state that the object is in rotation if best candidate has a harmonic within the list of candidates (or is a harmonic of another candidate). This hypothesis is based in two different contributions: the symmetries in the shape of the object and the repetition of *x* times the rotation pattern. In effect, the shape of an artificial satellite can be supposed to always have some type of symmetries (typically with respect to one or two planes), so that the rotation pattern in the signal can be split in *n* close identical sub-patterns, whose repetition frequencies will be found by the periodogram as harmonics of the real synodic rotation frequency of the object (typically x2 or x4, see blue result in Fig. 6). Additionally, when the rotation pattern is perfectly repeated from one rotation to other, the periodogram can also find the repetition frequency of a multiple of the real rotation pattern (typically twice), so at integer divisors of the real synodic rotation frequency of the object (typically /2, see green result in Fig. 6).

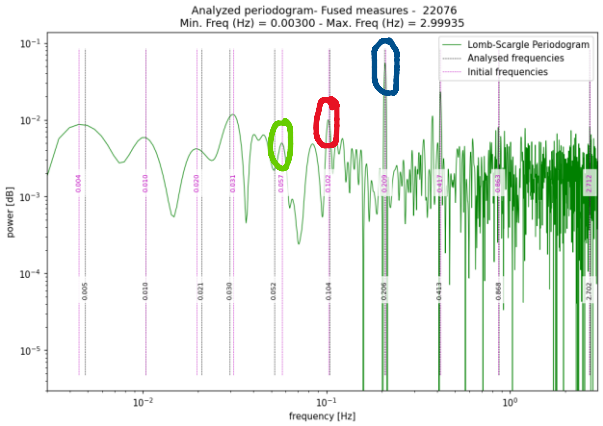

Satellite name = 22076

LIST OF THE FOLDED PERIODICITIES (CLASSIFIED ACCORDING TO THE STD ERROR)

Period (s)	Frequency (Hz)	Folding Error (ratio)	Signal type
9.64577	0.10367	1.270	LC
19.25013	0.05195	1.310	LC
33.61389	0.02975	1.418	LC
47.98698	0.02084	1.418	LC
96.31500	0.01038	1.454	LC
4.84622	0.20635	1.750	LC
1.15170	0.86828	3.186	LC
2.41923	0.41335	3.456	LC
0.37010	2.70195	3.516	LC

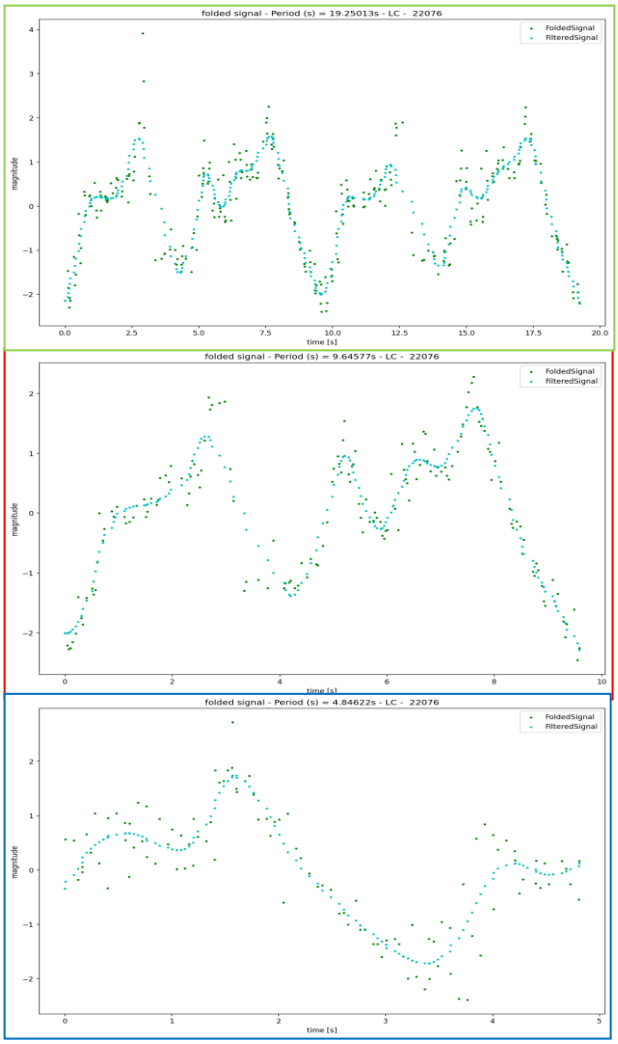

Fig. 6. Candidates selection and optimization for Topex (in tumbling at ~10 s period) using a light curve. Candidate in red is the real rotation frequency of the object. Candidate in blue is a harmonic (x2) due to Topex's shape one plane symmetry. Candidate in green is an integer divisor (/2) as periodogram find the repetition of twice the real rotation pattern. Candidate with the lowest folding error (first in results file) is the one corresponding to the real rotation period of the object.

However, it is important to note that the lack of a sequence of harmonics in the periodogram is not a warranty for 3-axis stabilization. This is because the periodogram can only detect a rotation frequency when the rotation pattern is at least seen twice during the observation. So, the only conclusion that can be stated in this case is that the object is not rotating with a period lower than half the duration of the observation.

5. Results

The validation of GLADIATOR is based on the analysis of the measurements obtained during a coordinated observations campaign lead by GMV and using 6 telescopes of 6Roads, CASTR radar at Chilbolton Observatory and the laser of Graz. This three-month campaign (from March to June 2022) has produced 33 days of effective observations of 57 3-axis stabilized objects (35 objects in LEO, 10 in MEO and 12 in GEO) and 22 rotating objects (6 objects in LEO, 12 in MEO and 4 in GEO). These objects and their characteristics are summarized in the annexed table at the end of this article (see Annexe A).

Observed objects have been carefully selected from free data available in [7,8,9,12] (see [10,11] for a description of MMT9 system), in order to only retain big (greater than 5 m considering solar arrays) 3-axis stabilized objects and rotating objects with a period lower than 100s (to ensure that short visibility slots in LEO can observe at least three rotations of the objects). Observations have been planned to maximize stereoscopies (object seen from different type of ground sensors at same time/day), performing observations at dawn and dusk and reducing the duration of each observation track in MEO/GEO to less than 10 minutes.

Every object has been analysed at every day of observation using the measurements of the day in five different ways: using classic light curve only, RCS only, laser range residuals only, laser light curve only and, finally, all types of measurements together. Every result is compared with the expected rotation state and rotation period of the object. This approach allows analysing the suitability of each type of measurement to determine the rotation state and the rotation rate of space objects, as well as the contribution of data fusion.

The criterion used to automatically classify an object as rotating is based on the presence of, at least, one integer multiplier or divisor of the best candidate (f_b) under order 5 within the list of analysed candidates (f_a). A maximum relative error of 2% is considered for integer multipliers and divisor detection:

$$\frac{r - round(r)}{round(r)} \cdot 100 < 2\%, \qquad round(r) < 5$$

, where r is checked twice for each analysed candidate: $r_1 = f_a/f_b$ and $r_2 = f_b/f_a$.

Fig. 7 shows the success rate determining that a 3-axis stabilized object is indeed not rotating. Success rate is always very close to 100% in all orbital regimes and using any type of measurement or fused data (ALL). The stereoscopic observations obtained were mostly limited to LEO regime (mainly classic light curves and RCS), so data fusion could not be evaluated in the other regimes. Laser range measurements could not be evaluated because of the small number of passes

obtained and the impossibility to compute residuals through an orbit determination process due to the reduced number of measurements in the passes.

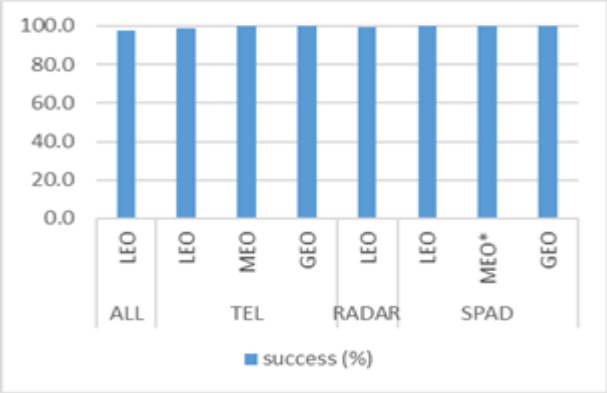

Fig. 7. Success rate determining the non-rotation of 3-axis stabilized satellites. SPAD means "Single Photon Avalanche Diode" and is used here for laser light curves measurements designation, as this is the instrument used to count received photons. * Not confident with value because of the small number of analyses performed.

Fig. 8 shows the success rate determining the rotation period of rotating objects with a 10% error (considering that reference values are not necessarily up to date and optimized). Classic light curves, RCS and their fusion (ALL) are very well suited for this purpose in LEO regime, with a success rate above 90%. Fusion seems to return worse results in LEO than telescopes or radars independently, but this is only because of the available sample for statistics computation: objects are less seen in stereoscopic observations than in observation with a single type of sensor. One can only see that success rate with classic and laser light curves decreases with orbital high, and this is mainly because of lower luminosity variations getting closer to measurement noise.

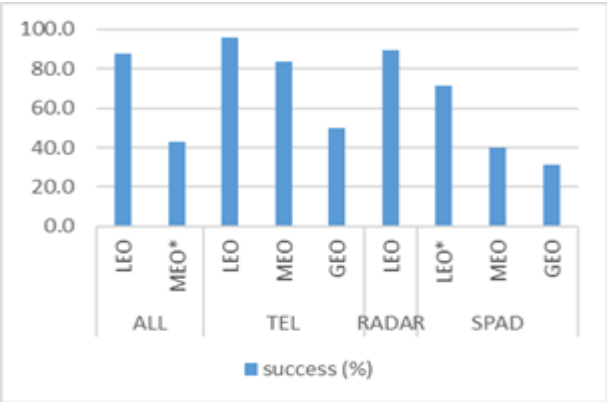

Fig. 8. Success rate determining the rotation period of rotating objects. * Not confident with value because of the small number of analyses performed.

Considering that reference values of rotation periods used for this validation could be out of date and not optimized, the precision of the tool in the determination of the synodic rotation period has been evaluated using simulated data. These data have been produced with another functionality of GLADIATOR using objects of different shapes (cylindrical rocket body, parallelepiped with one solar array, cube with two solar arrays), orbital regimes (LEO, MEO and GEO) and inertial rotation periods. In order to allow the comparison of the synodic rotation period obtained in the determination process with the inertial rotation period imposed in the simulation, only small inertial rotation periods ($\leq$ 10s) have been used in the validation. In all the cases, the rotation period of the object has been determined with an error lower than 1%. Using a real light curve from MMT9 database of a spin-stabilized satellite like METEOSAT 8 (MSG 1), whose rotation period is 0.6s, the error obtained in the determination process is 0.2%.

6. Conclusions

The tool implemented in this work (GLADIATOR) is capable of automatically determining the rotation state of an object. It can determine, using a single type of data or a fusion of different data, whether the object is rotating or 3-axis stabilized with a success rate close to 100% (assuming, for a rotating object, that data covers an interval of time of at least twice the rotation period of the object). It can also determine the synodic rotation period of a rotating object with an error lower than 1%. The performances of this tool, together with its automated processing, would allow its integration in a SST system in order to add attitude characterization and evolution to the catalogued objects.

Acknowledgements

The EU SST activities have received funding from the European Union programs, notably from the Horizon 2020 research and innovation program under grant agreements No 952852, No 785257, No 760459, No 713630 and No 713762, and the Copernicus and Galileo program under grant agreements No 299/G/GRO/COPE/19/11109, No 237/G/GRO/COPE/16/8935 and No 203/G/GRO/COPE/15/7987.

Mini-MegaTORTORA (MMT9) belongs to Kazan Federal University.

The authors wish to acknowledge the CASTR operations team at the UKRI/STFC Chilbolton Observatory, the Graz SLR operations team and 6Roads for conducting the observations for this work.

Annexe A: Characteristics of validation objects

OBJACT NAME	NORAD	OBJECT TYPE	ORBITAL REGIME	HAS RETROREFLECTOR?	ATTITUDE MODE	ROTATION PERIOD (s)
OPS 9845 (DMSP 5D-2 F6)	13736	PAY	LEO	NO	TUMBLING	16.79
DMSP 5D-2 F8 (USA 26)	18123	PAY	LEO	NO	TUMBLING	7.12
G44 / COSMOS 2079	20619	PAY	MEO	YES	TUMBLING	40.0 *
G47 / COSMOS 2109	21006	PAY	MEO	YES	TUMBLING	50.0 *
NOAA 12	21263	PAY	LEO	NO	TUMBLING	17.48
TOPEX	22076	PAY	LEO	YES	TUMBLING	9.77
NAVSTAR 36 (USA 100)	23027	PAY	MEO	YES	TUMBLING	3.03
G63 / COSMOS 2277	23044	PAY	MEO	YES	TUMBLING	45.0 *
G64 / COSMOS 2275	23045	PAY	MEO	YES	TUMBLING	70.0 *
G74 / COSMOS 2316	23620	PAY	MEO	YES	TUMBLING	35.0 *
G82 / COSMOS 2364	25593	PAY	MEO	YES	TUMBLING	75.0 *
G81 / COSMOS 2363	25594	PAY	MEO	YES	TUMBLING	65.0 *
G80 / COSMOS 2362	25595	PAY	MEO	YES	TUMBLING	70.0 *
GALAXY 27 (G-27)	25922	PAY	GEO	NO	TUMBLING	86.02
CZ-4B R/B	25942	R/B	LEO	NO	TUMBLING	8.91
TERRA	25994	PAY	LEO	NO	EARTH_POINT	
ASTRA 2B	26494	PAY	GEO	NO	EARTH_POINT	
NOAA 16	26536	PAY	LEO	NO	TUMBLING	4.47
ASTRA 2D	26638	PAY	GEO	NO	SPIN	1.1
G88 / COSMOS 2382	26987	PAY	MEO	YES	TUMBLING	50.0 *
G86 / COSMOS 2380	26989	PAY	MEO	YES	TUMBLING	80.0 *
TIMED	26998	PAY	LEO	NO	EARTH_POINT	
ASTRA 3A	27400	PAY	GEO	NO	EARTH_POINT	
AQUA	27424	PAY	LEO	NO	EARTH_POINT	
METEOSAT-8 (MSG-1)	27509	PAY	GEO	NO	SPIN	0.601
G93 / COSMOS 2404	28112	PAY	MEO	YES	TUMBLING	65.0 *
AURA	28376	PAY	LEO	NO	EARTH_POINT	
XTAR-EUR	28542	PAY	GEO	NO	EARTH_POINT	
CLOUDSAT	29107	PAY	LEO	NO	EARTH_POINT	
CALIPSO	29108	PAY	LEO	NO	EARTH_POINT	
HINODE (SOLAR-B)	29479	PAY	LEO	NO	SUN_POINT	
METOP-A	29499	PAY	LEO	NO	EARTH_POINT	
COROT	29678	PAY	LEO	NO	CHAOTIC	
WORLDVIEW-1 (WV-1)	32060	PAY	LEO	NO	EARTH_POINT	
ASTRA 1M	33436	PAY	GEO	NO	EARTH_POINT	
GOSAT (IBUKI)	33492	PAY	LEO	NO	EARTH_POINT	
NOAA 19	33591	PAY	LEO	NO	EARTH_POINT	
SMOS	36036	PAY	LEO	NO	EARTH_POINT	
COSMOS 2455	36095	PAY	LEO	NO	EARTH_POINT	
SDO	36395	PAY	GEO	NO	SUN_POINT	
ASTRA 3B	36581	PAY	GEO	NO	EARTH_POINT	
FENGYUN 3B	37214	PAY	LEO	NO	EARTH_POINT	
INTELSAT NEW DAWN	37392	PAY	GEO	NO	EARTH_POINT	
HYLAS 2	38741	PAY	GEO	NO	EARTH_POINT	

Annexe A: Characteristics of validation objects

OBJACT NAME	NORAD	OBJECT TYPE	ORBITAL REGIME	HAS RETROREFLECTOR?	ATTITUDE MODE	ROTATION PERIOD (s)
METOP-B	38771	PAY	LEO	NO	EARTH_POINT	
GSAT0103 (GALILEO-FM3)	38857	PAY	MEO	YES	EARTH_POINT	
GSAT0104 (GALILEO-FM4)	38858	PAY	MEO	YES	CHAOTIC	
COSMOS 2486	39177	PAY	LEO	NO	EARTH_POINT	
ES'HAIL 1	39233	PAY	GEO	NO	EARTH_POINT	
FENGYUN 3C	39260	PAY	LEO	NO	EARTH_POINT	
GPM-CORE	39574	PAY	LEO	NO	EARTH_POINT	
ALOS-2	39766	PAY	LEO	NO	EARTH_POINT	
METEOR-M 2	40069	PAY	LEO	NO	EARTH_POINT	
NAVSTAR 71 (USA 256)	40105	PAY	MEO	NO	EARTH_POINT	
NAVSTAR 72 (USA 258)	40294	PAY	MEO	NO	EARTH_POINT	
ASNARO	40298	PAY	LEO	NO	EARTH_POINT	
COSMOS 2502	40358	PAY	LEO	NO	EARTH_POINT	
EXPRESS-AM7	40505	PAY	GEO	NO	EARTH_POINT	
COSMOS 2506	40699	PAY	LEO	NO	EARTH_POINT	
NAVSTAR 74 (USA 262)	40730	PAY	MEO	NO	EARTH_POINT	
METEOSAT-11 (MSG-4)	40732	PAY	GEO	NO	SPIN	0.6
DAMPE	41173	PAY	LEO	NO	INERTIAL_POINT	
GSAT0209 (GALILEO 12)	41174	PAY	MEO	YES	CHAOTIC	
GSAT0208 (GALILEO 11)	41175	PAY	MEO	YES	EARTH_POINT	
EXPRESS-AMU1	41191	PAY	GEO	NO	EARTH_POINT	
JASON-3	41240	PAY	LEO	YES	EARTH_POINT	
NAVSTAR 76 (USA 266)	41328	PAY	MEO	NO	EARTH_POINT	
SENTINEL-3A	41335	PAY	LEO	YES	EARTH_POINT	
MICROSCOPE	41457	PAY	LEO	NO	EARTH_POINT	
QSS (MOZI)	41731	PAY	LEO	NO	INERTIAL_POINT	
GSAT0207 (GALILEO 15)	41859	PAY	MEO	YES	EARTH_POINT	
GSAT0212 (GALILEO 16)	41860	PAY	MEO	YES	EARTH_POINT	
GSAT0213 (GALILEO 17)	41861	PAY	MEO	YES	EARTH_POINT	
GSAT0214 (GALILEO 18)	41862	PAY	MEO	YES	EARTH_POINT	
HXMT (HUIYAN)	42758	PAY	LEO	NO	INERTIAL_POINT	
FENGYUN 3D	43010	PAY	LEO	NO	EARTH_POINT	
COSMOS 2524	43032	PAY	LEO	NO	EARTH_POINT	
SENTINEL-3B	43437	PAY	LEO	YES	EARTH_POINT	
PAKTES 1A	43529	PAY	LEO	NO	EARTH_POINT	
COSMOS 2528	43657	PAY	LEO	NO	EARTH_POINT	
GOSAT 2	43672	PAY	LEO	NO	EARTH_POINT	
METOP-C	43689	PAY	LEO	NO	EARTH_POINT	

* Tumbling period of Cosmos satellites is for year 2015 [12], as satellites with country code CIS are not shown in MMT9 database [9].

References

[1] K. Balachandran, K. Subbarao, Estimating Sidereal rotation period of Resident Space Objects using non-uniformly sampled light curves, 19th annual Advanced Maui Optical and Space Surveillance Technologies Conference (AMOS), Maui, USA, 2018, 11-14 September.

[2] D. Vallverdú Cabrera, J. Utzmann, R. Förstner, Integration of attitude characterization in a space debris catalogue using light curves, Proc. 8th European Conference on Space Debris, Darmstadt, Germany, 20–23 April 2021.

[3] Rita L. Cognion, Rotation rates of inactive satellites near geosynchronous earth orbit, annual Advanced Maui Optical and Space Surveillance Technologies Conference (AMOS), Maui, USA, 20148, 9-12 September.

[4] J. Silha, J. Pittet, M. Hamara, T. Schildknecht, Apparent rotation properties of space debris extracted from photometric measurements, Advances in Space Rersearch, Volume 61, Issue 3, 1 February 2018, Pages 844-861.

[5] D. Kucharski et al., Attitude and spin period of space debris Envisat measured by satellite laser ranging, IEEE Transactions on geoscience and remote sensing, Vol. 52, No. 12, December 2014.

[6] G. Kirchner, W. Hausleitner, E. Cristea, Ajisai spin parameter determination using Graz kilohertz satellite laser ranging data, IEEE Transactions on geoscience and remote sensing, Vol. 45, No. 1, January 2007.

[7] CelesTrack catalogue: https://celestrak.org/.

[8] Jonathan C. MacDowell's General Catalogue of Artifical Space Objects: https://planet4589.org/space/gcat/.

[9] MMT9 database of light curves and analysed periodicities of space objects: http://mmt9.ru/satellites/.

[10] Karpov et al., Massive photometry of low-altitude artificial satellites on Mini-Mega-TORTORA, Revista Mexicana de Astronomía y Astrofísica (Serie de Conferencias) Vol. 48, pp. 112-113 (2016).

[11] Beskin et al., Wide-field optical monitoring with Mini-MegaTORTORA (MMT-9) multichannel high temporal resolution telescope, Astrophysical Bulletin, Volume 72, Issue 1, pp.81-92.

[12] M. Steindorfer, G. Kirchner, F. Koidl, P. Wang, Light curve measurements with single photon counters at Graz SLR, ILRS Technical Workshop, Matera, Italy, October 2015.